Evidence of the direct-to-indirect band gap transition in strained two-dimensional WS$_2$, MoS$_2$, and WSe$_2$

E. Blundo,[1] M. Felici [ORCID],[1] T. Yildirim,[2] G. Pettinari [ORCID],[3] D. Tedeschi,[1] A. Miriametro,[1] B. Liu,[2] W. Ma [ORCID],[2] Y. Lu [ORCID],[2,4] and A. Polimeni [ORCID][1,*]

[1]*Dipartimento di Fisica, Sapienza Università di Roma, 00185 Roma, Italy*

[2]*Research School of Electrical, Energy and Materials Engineering, College of Engineering and Computer Science,*
The Australian National University, Canberra, ACT 2601, Australia

[3]*Institute for Photonics and Nanotechnologies, National Research Council, 00156 Roma, Italy*

[4]*ARC Centre of Excellence in Future Low-Energy Electronics Technologies (FLEET) ANU node, Canberra, ACT 2601, Australia*

We report a strain-induced direct-to-indirect band gap transition in mechanically deformed WS$_2$ monolayers (MLs). The necessary amount of strain is attained by proton irradiation of bulk WS$_2$ and the ensuing formation of 1-ML-thick, H$_2$-filled domes. The electronic properties of the curved MLs are mapped by spatially and time-resolved microphotoluminescence, revealing the mechanical stress conditions that trigger the variation of the band gap character. This general phenomenon, also observed in MoS$_2$ and WSe$_2$, further increases our understanding of the electronic structure of transition metal dichalcogenide MLs and holds a great relevance for their optoelectronic applications.

The properties of solids are very sensitive to variations in bond length ensuing a mechanical deformation or stress. This is especially true in the case of two-dimensional (2D) crystals [such as graphene, hexagonal-BN, and transition metal dichalcogenide (TMD) monolayers (MLs)] due to their all-surface nature [1]. Particularly appealing in TMD MLs is the strong coupling between the valley/spin/orbital degrees of freedom and the lattice structure, reflected in the strong response of their electronic [2], transport [3], and optical [4] properties to strain. In particular, nonuniform strains turn out to be extremely relevant: On the one hand, strain gradients in 2D TMDs can lead to a coherent drift of photogenerated carriers, relevant for photon harvesting [5,6]. On the other hand, a nonuniform strain gives rise to pseudoelectromagnetic fields enabling the observation of novel transport phenomena [7].

In this Rapid Communication, we report a study of the band gap character in mechanically deformed WS$_2$, MoS$_2$, and WSe$_2$ 2D crystals. The deformation follows the local blistering over a micron-sized region of the upper layer of bulk flakes exposed to proton irradiation [8]. The resulting spherically shaped MLs, hereafter named domes, host nonuniform and high strain fields, evaluated by finite-element method (FEM) calculations and consistently compared with micro-Raman measurements. Steady-state and time-resolved microphotoluminescence (micro-PL) mapping of the band gap states over the surface of a single dome unveils dramatic changes in the emission energy, intensity, and decay time.

*Corresponding author: antonio.polimeni@roma1.infn.it

Such changes are related to the built-in tensile strain of the dome and are ascribed to a strain-induced direct (K_{CB}-K_{VB})-to-indirect (K_{CB}-Γ_{VB}) band gap transition (CB and VB stand for conduction and valence band, respectively). The strain conditions that determine the crossover of the VB Γ and K states are found.

The dome-shaped membranes under study were created from bulk MX_2 flakes (where $M = $ W or Mo, and $X = $ S, Se, or Te), which were mechanically exfoliated on Si substrates and then proton irradiated with a low-energy beam [8,9]. Here, we focus on WS$_2$. The accelerated protons penetrate through the flake surface and H$_2$ forms just one layer beneath the surface, as described in Ref. [8]. As a consequence of the balance between the gas expansion, the van der Waals forces holding the S-W-S planes together and the material's elastic properties, localized swelling of just 1 ML takes place, resulting in the formation of atomically thin and spherically shaped domes [see the atomic force microscope (AFM) image in Fig. 1(a)]. The domes cage highly pressurized H$_2$ and are durable owing to the impermeability to H$_2$ of TMD MLs [10]. As shown in Fig. 1(a), domes with different size stud the flake's surface, nevertheless featuring an aspect ratio, $h_m/R = 0.16 \pm 0.02$, independent of R [8,11] (R is the footprint radius and h_m is the maximum height of the domes). The domes were characterized by micro-Raman and micro-PL experiments at room temperature using a 532-nm laser as the excitation source. A diffraction grating monochromator coupled to a Si-CCD was used for spectral analysis of the signal. Time-resolved micro-PL at 50 K was performed using a supercontinuum laser tuned at 532 nm with ~50 ps pulse width and 77.8 MHz repetition rate. The signal was time analyzed by a Si avalanche photodiode (APD) with 250 ps temporal resolution. Spatially resolved optical measurements were performed in backscattering configuration via a 100×
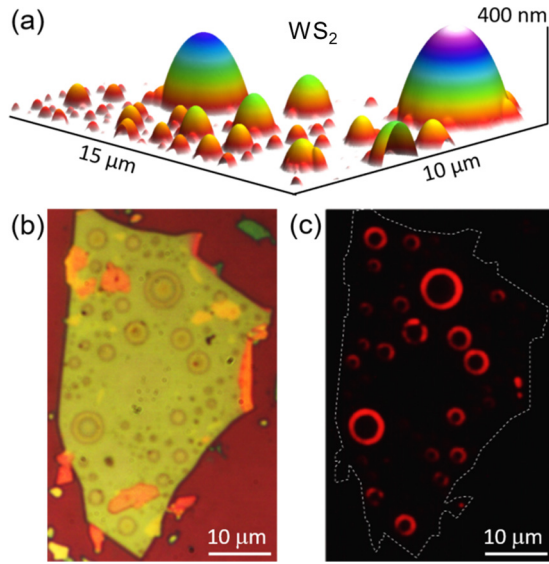
FIG. 1. (a) 3D AFM image of a bulk WS_2 flake irradiated with protons (dose $d_H = 4 \times 10^{16}$ protons/cm^2), showing the formation of almost perfectly spherical domes. (b) Optical image of a WS_2 flake, where many relatively large domes formed after proton irradiation ($d_H = 5 \times 10^{16}$ protons/cm^2). (c) Laser-excited red luminescence coming from the same flake shown in (b).

objective with numerical aperture (NA) = 0.9, resulting in a laser spot with a standard deviation equal to $0.23 \pm 0.01 \, \mu m$ [12]. Finally, the strain tensor over the dome's surface was computed via FEM calculations [8].

Figure 1(b) shows the optical microscope image of a proton-irradiated WS_2 flake acquired with a $50 \times$ (NA = 0.5) objective. The outer circular borders locate the domes' footprint while the internal patterns of each dome are due to interference effects between the light reflected by the dome top surface and the flat WS_2 flake underneath [8]. Figure 1(c) shows an optical image of the same flake, excited by a defocused 532-nm laser. The image was acquired at room temperature by filtering out the laser, thus letting the red luminescence (at $\sim$690 nm) generated by the domes be revealed. Peculiarly, the brightly emitting region is restricted to an outer ringlike area independently of the dome footprint. This excludes interference (which would be largely dependent on the dome size) to be the main origin of the observed luminescence pattern, differently from what recently reported in WS_2 bubbles obtained after annealing of chemical-vapor-deposition-grown MLs [13]. In that work, interference effects are likely enhanced by the SiO_2 substrate located right beneath the ML bubbles and strongly modulate the emission. On the contrary, in the present case, the peculiar ringlike emitting area stems from the strain field acting over the domes, as detailed in the following.

To model the spatial evolution of the strain tensor and the height profile of the domes we performed FEM calculations within the framework of the nonlinear membrane theory [8,14,15]. The AFM-derived radius and height of the domes and the elastic properties of the material were used as input parameters. Figure 2(a) (left axis) successfully compares the experimental (circles) and calculated (solid line) height profile along a radius ($0 \leqslant r \leqslant R$, where r is the position with
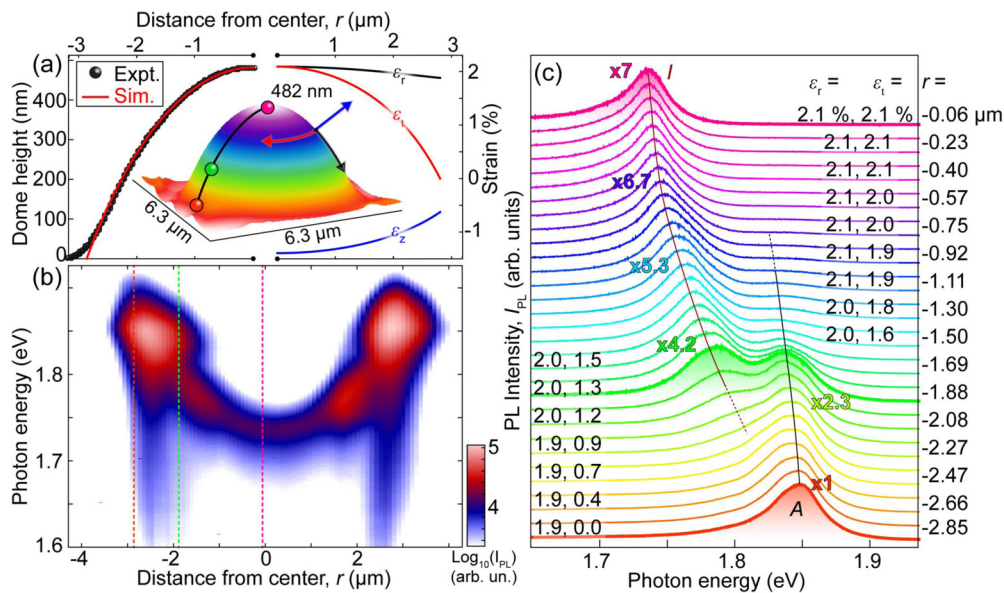

FIG. 2. (a) Left: Height profile of a WS_2 dome formed after irradiation with 4×10^{16} protons/cm^2, measured by AFM (black dots; the AFM image is shown as inset), and computed by FEM calculations (solid red line). Right: Dependence along the dome radius of the strain tensor components, represented as color-coded arrows in the inset. The three dots (purple: top; green: intermediate; orange: edge) correspond to the positions displayed as dashed lines in (b) and to the shadowed spectra in (c). (b) Micro-PL scan (with steps of 80 nm) along a diameter of the dome displayed in (a), performed at 297 K. The horizontal axis indicates the laser spot position with respect to the dome center, and the vertical axis indicates the emitted photon energy. The base-10 logarithm of the micro-PL intensity is shown in a false color scale. (c) Normalized emission spectra of the dome as the laser spot is scanned from the dome's left edge (bottom) to its apex (top). Intensity factors are displayed for some selected spectra. Spectra are labeled with the laser spot position and with the values of the radial (ε_r) and circumferential (ε_t) strain components. The solid lines follow the energy shift of the direct (A, black line) and indirect (I, red line) exciton transition.

respect to the center) of the WS$_2$ dome, whose AFM image is shown in the inset. The right axis of Fig. 2(a) displays the calculated r dependence of the principal components of the strain tensor—namely, along the circumferential (ε_t) and radial (ε_r) in-plane directions [14] and along the perpendicular (ε_z) out-of-plane direction. At the dome's summit, the (tensile) strain is isotropic biaxial ($\varepsilon_t = \varepsilon_r = 2.09\%$), in agreement with Hencky's model [4,8,14,16], whereas at the dome edges—where $\varepsilon_t = 0$—strain is uniaxial. The negative value of ε_z all over the surface is caused by the membrane thinning following the in-plane tensile strain. The strain field across the dome is expected to induce remarkable changes in the electronic properties of the curved TMD membrane [5,17–27], giving rise to the peculiar phenomenology displayed in Fig. 1(c). Spatially resolved micro-PL/Raman measurements were then performed on the dome shown in Fig. 2(a), which was chosen since its size ($R = 2.85 \, \mu$m) is much larger than the probing laser spot (0.23 μm) [12], thus minimizing diffraction effects. However, it is important to note that the dome aspect ratio and, consequently, the strain distribution remain unchanged with the dome size [8], ensuring the general significance of the following results.

To begin with, the micro-Raman measurements described in the Supplemental Material [28] show a progressive softening of the in-plane and out-of-plane vibrational modes while moving from the edge towards the center of the dome, in agreement with the expected tensile-strain increase [13,29,30]. However, the full extent of the effects of strain on the optoelectronic properties of TMD MLs can only be appreciated by looking at the dome's PL emission. Figure 2(b) depicts a room-temperature micro-PL scan taken along a diameter of the dome displayed in the inset of Fig. 2(a). The vertical axis indicates the energy of the emitted photons, while the base-10 logarithm of the PL intensity is shown in a false color scale. On moving from the edge toward the summit of the dome, the marked redshift of the emission wavelength is accompanied by an equally striking decrease (about a factor 10) of the PL intensity. Figure 2(c) describes in more detail the dramatic changes of the emission spectra from the dome's edge ($r = -2.85 \, \mu$m) to the dome's center ($r = -0.06 \, \mu$m). Each spectrum is labeled also with the pertinent values of the radial and circumferential strain components [see Fig. 2(a)]. The micro-PL spectra recorded close to the edge are dominated by the direct (K_{CB}-K_{VB}) band gap exciton (A), whose energy (equal to 2.00 eV in a strain-free reference WS$_2$ ML [8]) is redshifted by the tensile strain exerted on the dome. As the excitation laser moves toward the center, the direct exciton keeps redshifting and concomitantly a new, less intense band, labeled I, takes over and eventually dominates the spectrum. We ascribe this band to the K_{CB}-Γ_{VB} *indirect* band gap exciton. In fact, as predicted by numerous theoretical works [5,17,18,20–24], the presence of strain in TMD MLs [17,18,20–25,27] and bilayers [31,32] should result in a significant reordering of the energies of the critical points of the band structure. In particular, for tensile biaxial strains $\varepsilon > 1\%$ in WS$_2$ MLs [17,18,20–22,24,25,27], the valence band maximum should change from the K to the Γ point of the reciprocal space. Even though this change (i) is expected to occur for values of ε that are well within reach of current strain modulation techniques [31,33–35], and (ii) should result in
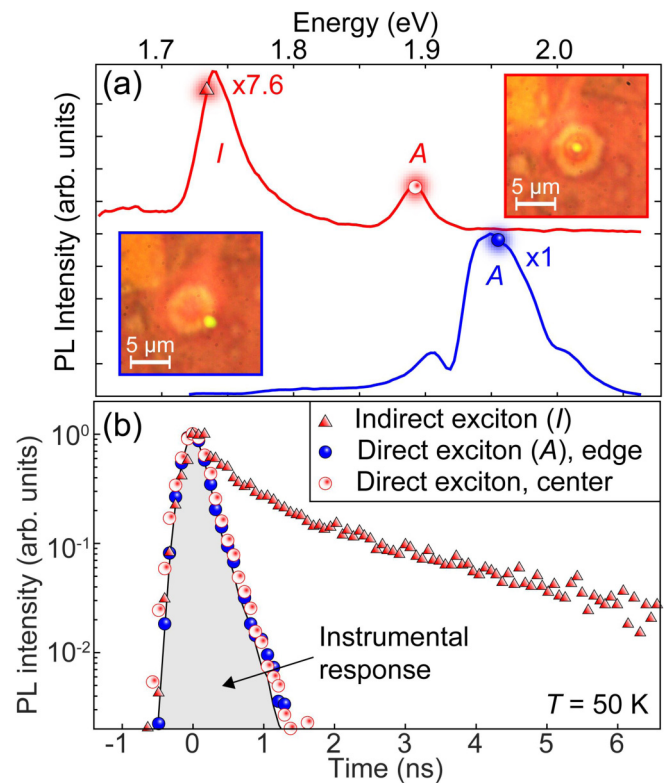

FIG. 3. (a) $T = 50$ K micro-PL spectra recorded at the center (red) and edge (blue) of a WS$_2$ dome. The insets are optical microscope images of the dome, showing the laser spot position corresponding to each spectrum. The symbols superimposed on the spectra indicate the energy at which the signal temporal decay shown in (b) was recorded. (b) Temporal evolution of the micro-PL signal relative to the specific photon energy and position on the dome highlighted in (a). The gray-shaded area refers to the exciting laser decay curve and sets the temporal resolution.

rather dramatic variations of the optical properties of the material, the currently available experimental evidence of this direct-to-indirect transition is either not particularly apparent [36–39] or absent [13,34,35,31]. This is possibly due to a less-than-perfect adhesion between the sample and the strain-inducing devices employed in some of the previous studies, resulting in an incomplete transfer of the applied stress to the TMD ML. In the present work, however, this is not an issue, as large biaxial strains—in the range between 1% and 3%—are induced by the pressure exerted on the TMD ML by the H$_2$ gas trapped and perfectly sealed within the dome.

To confirm the previous attributions, we investigated the temporal decay of the micro-PL signal of WS$_2$ domes. These were cooled down at 50 K to minimize the contribution of nonradiative decay channels [40]. Interestingly, the reduction of the dome's volume at cryogenic temperatures [8]—due to the contraction of the H$_2$ gas trapped inside the dome—is nearly brought to a halt by the deposition of a thin methylpentane layer on the sample surface (see Supplemental Material [28]), thus making it possible to spatially resolve the PL signal from different zones of the dome. Figure 3(a) shows the micro-PL spectra of a WS$_2$ dome recorded at the edge (where the A exciton dominates) and center (where the I

exciton can be observed along with the redshifted *A* exciton recombination); see pictures in the insets. Figure 3(b) shows the micro-PL decay curve relative to the different transitions displayed in Fig. 3(a). Most notably, the *A* and *I* excitons exhibit largely different temporal behaviors: The decay time of the *A* exciton is instrument limited (<250 ps), consistent with other reports [40,41]. Instead, the *I* exciton shows a much longer temporal decay that can be fitted by a double exponential function with two decay times equal to (0.40 ± 0.06) ns and (2.9 ± 0.7) ns, which clearly points to an indirect optical transition [41].

We now establish the strain conditions that induce the K-Γ crossover in the VB. This is an especially important aspect with regard to the optoelectronic properties of TMD MLs and to the enormous potential that mechanical stress holds to engineer those properties. For instance, application of a seamless gradient of strain in these materials could be exploited as an efficient broadband concentrator of photogenerated carriers in flexible solar cells [5]. Nevertheless, the occurrence of a strain-induced transition in the band gap character may affect both the absorption/emission properties and the carrier dynamics characteristics of devices based on TMD MLs. Furthermore, in the present case, the strain gradient enables the spatial concentration of long-lived k-indirect excitons with potential benefit for creating excitonic Bose condensates [42].

Figure 4(a) illustrates a micro-PL experiment performed on a single dome, highlighting the relevant physical processes discussed next. Figure 4(b) shows the peak energy $E_{A,I}$ of the *A* and *I* excitonic transitions derived from the same dome of Fig. 2 as a function of the "in-plane" strain $\varepsilon_\mathrm{p} = \varepsilon_\mathrm{r} + \varepsilon_\mathrm{t}$. This choice is grounded on the hypothesis that each of the two planar strain components brings a similar effect on the ML band gap [17]. Moreover, for biaxially strained TMDs, $\varepsilon_\mathrm{z} = -\frac{D_{13}}{D_{33}}\varepsilon_\mathrm{p}$, where D_{13} and D_{33} are the pertinent components of the elasticity matrix [8,43]. Thus, as discussed in the Supplemental Material [28] the strain dependence of the energies of the *A* and *I* excitons can be written as

$$E_{A,I}(\varepsilon_\mathrm{p}) = E_{A,I}(0) - \Delta_{A,I}\varepsilon_\mathrm{p}, \qquad (1)$$

where $\Delta_{A,I}$ is the shift rate with strain of the *A* (*I*) exciton. To correctly interpret the data shown in Fig. 4(b), however, we also have to consider that the continuous variation of the strain field on the dome surface [Fig. 2(a)]—and hence the progressive decrease of the band gap energy from the dome edge toward its center—leads excitons to drift toward the minimum energy available within their diffusion length before recombining [see Fig. 4(a)] [5,6].

Such a funnel effect, combined with the finite exciting/collecting area of the objective, alters the correspondence between the coordinate r (and thus ε_p) and the exciton energy derived from the emission spectra [6]. The solid curves displayed in Fig. 4(b) result from a fit performed by taking into account the exciton funneling (see Supplemental Material [28]), while fixing the radius of the collection area R_c to 2.5σ ($\sigma = 0.23$ μm is the laser spot size [12]). The actual [i.e., free from the funnel effect; see Eq. (1)], "linearized" strain dependence of the *A* (*I*) exciton is shown in Fig. 4(b) as a blue (red) dashed line [44]. The surrounding shaded areas—covering the regions spanned by the trends computed for $2\sigma \leqslant R_c \leqslant 3\sigma$—represent the uncertainty of our
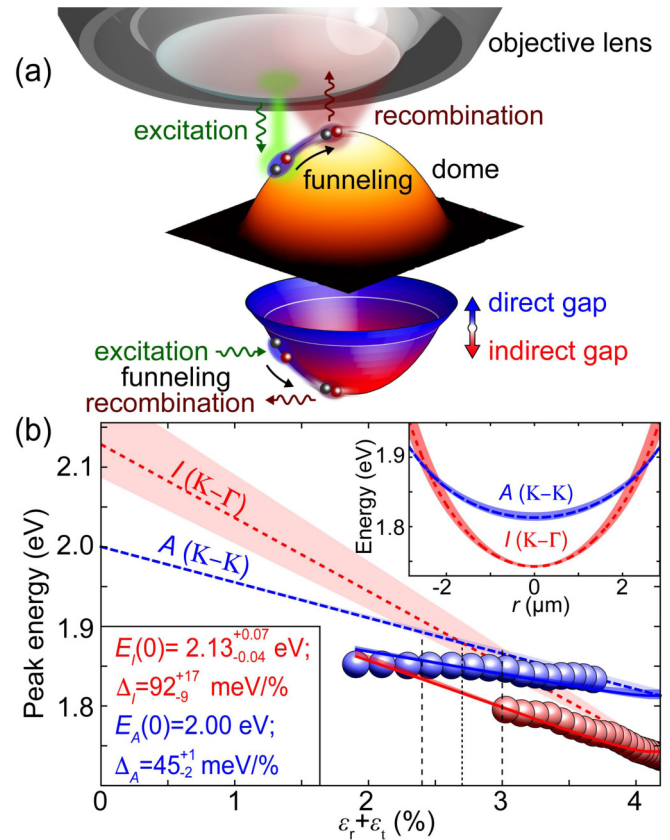

FIG. 4. (a) Sketch of a micro-PL experiment (excitation+recombination) on a single WS$_2$ dome (whose AFM image is shown in shaded orange), wherein an exciton drifts over the dome strain distribution (funnel effect [5,6]). The blue-red paraboloid provides a correspondence between the dome AFM image and the exciton energy, highlighting the direct-indirect transition region (see below). (b) Dependence of the energy of the direct (blue dots) and indirect (red dots) exciton transitions on the in-plane strain tensor, $\varepsilon_\mathrm{p} = \varepsilon_\mathrm{r} + \varepsilon_\mathrm{t}$. The solid blue/red lines (relative to the direct/indirect exciton) are fits based on Eq. (1), while also taking funneling [see (a)] into account. These fits entail linear dependences of the exciton energies on ε_p, which are displayed as dashed lines; the shaded areas enveloping each curve account for the uncertainty of our fitting procedure (see main text). In turn, these linear dependences yield the evolution of the direct and indirect exciton energy across the dome, plotted in the inset of (b) [the paraboloid sketched in (a) is also based on this evolution].

procedure. This analysis permits to set the direct-to-indirect band gap crossover point at $\varepsilon_\mathrm{p} = (2.7 \pm 0.3)\%$ highlighted by vertical dashed lines in Fig. 4(b). Finally, the top-right inset in Fig. 4(b) provides the *A* and *I* exciton energy as a function of the dome radial coordinate. The displayed fits yield $\Delta_A = 45^{+1}_{-2}$ meV/$\varepsilon\%$, $E_I(0) = 2.13^{+0.07}_{-0.04}$ eV and $\Delta_I = 92^{+17}_{-9}$ meV/$\varepsilon\%$ [$E_A(0)$ is fixed to 2.00 eV, the strain-free ML exciton energy]. These data compare rather favorably with the experimental [35,45], and theoretical [17,18,20–22,24–27,46] ones as reported in Table I. However, we notice a large discrepancy between the $E_I(0)$-$E_A(0)$ value derived in this work (130 meV) and those reported in other works. In fact, these latter estimate the electronic band gap whereas our

TABLE I. Comparison between the data reported in this work and those in different experimental (Expt.) and theoretical (Theor.) works. $\Delta_{A(I)}$ indicates the shift rate with strain of the A (I) exciton energy. $E_I(0)$-$E_A(0)$ is the indirect-direct exciton energy difference at zero strain (though this quantity in the other works corresponds to the difference of the electronic band gap). $\varepsilon_{\text{transition}}$ is the equivalent uniaxial strain at which the band gap turns indirect.

		Our work	Expt. works	Theor. works
WS$_2$	Δ_A (meV/%)	45^{+1}_{-2}	46 [45], 47 [35]	59 [21], 67 [27], 66−75 [20]
	Δ_I/Δ_A	2.0		1.8−1.9 [20], 1.9 [27], 2.0 [21]
	$E_I(0)$-$E_A(0)$ (meV)	130^{+70}_{-40}	(280 ± 10) [26]	77 [21], 173 [46], 242 [20], 274 [27]
	$\varepsilon_{\text{transition}}$ (%)	2.7 ± 0.3		$\geqslant 2$ [17,19,20,22,24,25,27]
MoS$_2$	Δ_A (meV/%)	37^{+3}_{-1}	(45 ± 3) [4], (45 ± 7) [32]	47 [21], 52−61 [20], 66 [27]
	Δ_I/Δ_A	2.5		2.0 [21], 2.1 [27], 2.3 [20]
	$E_I(0)$-$E_A(0)$ (meV)	100^{+80}_{-50}	~ 300 [49]	13 [21], 110 [27], 127−184 [20], 148 [46]
	$\varepsilon_{\text{transition}}$ (%)	1.8 ± 0.7		$\geqslant 0.1$ [5,17,19−21,23−25,27,32]

data embed exciton effects that are quite different for the A and I transitions: A heavier hole effective mass is reported in Ref. [26] at Γ ($m_\Gamma^h = 2.45m_0$, m_0 is the electron mass in vacuum) compared to K ($m_K^h = 0.48m_0$) that results in a difference between the indirect and direct exciton binding energy [47] equal to $+144$ meV [48]. In turn, this brings our 130 meV exciton value to a 274 meV electronic value, in close agreement with the other works' reported in Table I. We finally point out that we observed similar findings also in MoS$_2$ (see Table I) and WSe$_2$ [28].

In conclusion, we investigated the intertwined strain and electronic properties of spherically deformed TMD monolayers. We observed that sufficiently high tensile in-plane strains ($\varepsilon_p \sim 2.7\%$ in WS$_2$ ML, $\varepsilon_p \sim 1.5\%$ in MoS$_2$ ML, $\varepsilon_p \sim 2\%-3\%$ in WSe$_2$ ML [28]) turn a direct band gap material into an indirect-gap one. This general behavior must be considered when 2D crystals are to be employed in flexible optoelectronic devices, or possibly exploited for the observation of quantum many-body effects involving long-lived k-space indirect excitons [42].

[1] Z. Dai, L. Liu, and Z. Zhang, Strain engineering of 2D materials: Issues and opportunities at the interface, Adv. Mater. **31**, 1805417 (2019).

[2] B. Amorim, A. Cortijo, F. de Juan, A. G. Grushin, F. Guinea, A. Gutiérrez-Rubio, H. Ochoa, V. Parente, R. Roldán, P. San-Jose, J. Schiefele, M. Sturla, and M. A. H. Vozmediano, Novel effects of strains in graphene and other two dimensional materials, Phys. Rep. **617**, 1 (2016).

[3] S. Deng, A. V. Sumant, and V. Berry, Nano Today **22**, 14 (2018).

[4] D. Lloyd, X. Liu, J. W. Christopher, L. Cantley, A. Wadehra, B. L. Kim, B. B. Goldberg, A. K. Swan, and J. S. Bunch, Band gap engineering with ultralarge biaxial strains in suspended monolayer MoS$_2$, Nano Lett. **16**, 5836 (2016).

[5] J. Feng, X. Qian, C.-W. Huang, and J. Li, Strain-engineered artificial atom as a broad-spectrum solar energy funnel, Nat. Photonics **6**, 866 (2012).

[6] A. Castellanos-Gomez, R. Roldan, E. Cappelluti, M. Buscema, F. Guinea, H. S. J. van der Zant, and G. A. Steele, Local strain engineering in atomically thin MoS$_2$, Nano Lett. **13**, 5361 (2013).

[7] H. Ochoa, R. Zarzuela, and Y. Tserkovnyak, Emergent gauge fields from curvature in single layers of transition-metal dichalcogenides, Phys. Rev. Lett. **118**, 026801 (2017).

[8] D. Tedeschi, E. Blundo, M. Felici, G. Pettinari, B. Liu, T. Yildrim, E. Petroni, C. Zhang, Y. Zhu, S. Sennato, Y. Lu, and A. Polimeni, Controlled micro/nanodome formation in proton-irradiated bulk transition-metal dichalcogenides, Adv. Mater. **31**, 1903795 (2019).

[9] R. Trotta, A. Polimeni, F. Martelli, G. Pettinari, M. Capizzi, L. Felisari, S. Rubini, M. Francardi, A. Gerardino, P. C. M. Christianen, and J. C. Maan, Fabrication of site-controlled quantum dots by spatially selective incorporation of hydrogen in Ga(AsN)/GaAs heterostructures, Adv. Mater. **23**, 2706 (2011).

[10] M. Seel and R. Pandey, Proton and hydrogen transport through two-dimensional monolayers, 2D Mater. **3**, 025004 (2016).

[11] E. Khestanova, F. Guinea, L. Fumagalli, A. Geim, and I. Grigorieva, Universal shape and pressure inside bubbles appearing in van der Waals heterostructures, Nat. Commun. **7**, 12587. (2016).

[12] The laser spot size resulting from the NA = 0.9 objective employed for micro-Raman and micro-PL mapping was experimentally determined as follows: The laser was scanned across a reference sample, lithographically patterned with features of known width (1 μm). The intensity of the reflected light was fitted with the ideal reflectance profile, convolved with a Gaussian

peak. The standard deviation of this peak, obtained as a fitting parameter, provides our estimate of $\sigma = 0.23 \pm 0.01 \ \mu m$.

[13] Z. Jia, J. Dong, L. Liu, A. Nie, J. Xiang, B. Wang, F. Wen, C. Mu, Z. Zhao, B. Xu, Y. Gong, Y. Tian, and Z. Liu, Photoluminescence and Raman spectra oscillations induced by laser interference in annealing-created monolayer WS₂ bubbles, Adv. Opt. Mater. **7**, 1801373 (2019).

[14] K. Yue, W. Gao, R. Huang, and K. M. Liechti, Analytical methods for the mechanics of graphene bubbles, J. Appl. Phys. **112**, 083512 (2012).

[15] P. Wang, W. Gao, Z. Cao, K. M. Liechti, and R. Huang, Numerical analysis of circular graphene bubbles, J. Appl. Mech. **80**, 040905 (2013).

[16] W. B. Fichter, Some solutions for the large detections of uniformly loaded circular membranes, NASA Technical Report No. NASA-TP-3658, 1997 (unpublished).

[17] P. Johari and V. B. Shenoy, Tuning the electronic properties of semiconducting transition metal dichalcogenides by applying mechanical strains, ACS Nano **6**, 5449 (2012).

[18] S. Horzum, H. Sahin, S. Cahangirov, P. Cudazzo, A. Rubio, T. Serin, and F. M. Peeters, Phonon softening and direct to indirect band gap crossover in strained single-layer MoSe₂, Phys. Rev. B **87**, 125415 (2013).

[19] M. Ghorbani-Asl, S. Borini, A. Kuc, and T. Heine, Strain-dependent modulation on conductivity in single-layer transition-metal dichalcogenides, Phys. Rev. B **87**, 235434 (2013).

[20] H. Shi, H. Pan, Y.-W. Zhang, and B. I. Yakobson, Quasiparticle band structures and optical properties of strained monolayer MoS₂ and WS₂, Phys. Rev. B **87**, 155304 (2013).

[21] C.-H. Chang, X. Fan, S.-H. Lin, and J.-L. Kuo, Orbital analysis of electronic structure and phonon dispersion in MoS₂, MoSe₂, WS₂, and WSe₂ monolayers under strain, Phys. Rev. B **88**, 195420 (2013).

[22] B. Amin, T. P. Kaloni, and U. Schwingenschl, Strain engineering of WS₂, WSe₂, and WTe₂, RCS Adv. **4**, 34561 (2014).

[23] R. Das, B. Rakshit, S. Debnath, and P. Mahadevan, Microscopic model for the strain-driven direct to indirect band-gap transition in monolayer MoS₂ and ZnO, Phys. Rev. B **89**, 115201 (2014).

[24] L. Ortenzi, L. Pietronero, and E. Cappelluti, Zero-point motion and direct-indirect band-gap crossover in layered transition-metal dichalcogenides, Phys. Rev. B **98**, 195313 (2018).

[25] L. Wang, A. Kutana, and B. I. Yakobson, Many-body and spin-orbit effects on direct-indirect band gap transition of strained monolayer MoS₂ and WS₂, Ann. Phys. **526**, L7 (2014).

[26] L. Waldecker, A. Raja, M. Rösner, C. Steinke, A. Bstwick, R. J. Koch, C. Jozwiak, T. Taniguchi, K. Watanabe, E. Rotenberg, T. O. Wehling, and T. F. Heinz, Rigid Band Shifts in Two-Dimensional Semiconductors through External Dielectric Screening, Phys. Rev. Lett. **123**, 206403 (2019).

[27] K. Zollner, P. E. Faria Junior, and J. Fabian, Strain-tunable orbital, spin-orbit, and optical properties of monolayer transition-metal dichalcogenides, Phys. Rev. B **100**, 195126 (2019).

[28] See Supplemental Material at http://link.aps.org/supplemental/10.1103/PhysRevResearch.2.012024 for a detailed description of micro-Raman experiments, effect of dome capping on the dome volume versus T, funneling effect details, and results found in other 2D TMDs.

[29] F. Wang, I. A. Kinloch, D. Wolverson, R. Tenne, A. Zak, E. O'Connell, U. Bangert, and R. J. Young, Strain-induced phonon

[30] A. M. Dadgar, D. Scullion, K. Kang, D. Esposito, E.-H. Yang, I. P. Herman, M. A. Pimenta, E.-J. G. Santos, and A. N. Pasupathy, Achieving large, tunable strain in monolayer transition-metal dichalcogenides, Chem. Mater. **30**, 5148 (2018).

[31] S. B. Desai, G. Seol, J. S. Kang, H. Fang, C. Battaglia, R. Kapadia, J. W. Ager, J. Guo, and A. Javey, Strain-induced indirect to direct bandgap transition in multilayer WSe₂, Nano Lett. **14**, 4592 (2014).

[32] H. J. Conley, B. Wang, J. I. Ziegler, R. F. Haglund, Jr., S. T. Pantelides, and K. I. Bolotin, Bandgap engineering of strained monolayer and bilayer MoS₂, Nano Lett. **13**, 3626 (2013).

[33] Q. Zhang, Z. Chang, G. Xu, Z. Wang, Y. Zhang, Z.-Q. Xu, S. Chen, Q. Bao, J. Z. Liu, Y.-W. Mai, W. Duan, M. S. Fuhrer, and C. Zheng, Strain relaxation of monolayer WS₂ on plastic substrate, Adv. Funct. Mater. **26**, 8707 (2016).

[34] R. Yang, J. Lee, S. Ghosh, H. Tang, R. M. Sankaran, C. A. Zorman, and P. X.-L. Feng, Tuning optical signatures of single- and few-layer MoS₂ by blown-bubble bulge straining up to fracture, Nano Lett. **17**, 4568 (2017).

[35] R. Frisenda, M. Drüppel, R. Schmidt, S. M. de Vasconcellos, D. P. de Lara, R. Bratschitsch, M. Rohlfing, and A. Castellanos-Gomez, Biaxial strain tuning of the optical properties of single-layer transition metal dichalcogenides, 2D Mater. **1**, 10 (2017).

[36] J. Chaste, A. Missaoui, S. Huang, H. Henck, Z. Ben Aziza, L. Ferlazzo, C. Naylor, A. Balan, A. T. C. Johnson, Jr., R. Braive, and A. Ouerghi, Intrinsic Properties of suspended MoS₂ on SiO₂/Si pillar arrays for nanomechanics and optics, ACS Nano **12**, 3235 (2018).

[37] Y. Wang, C. Cong, W. Yang, J. Shang, N. Peimyoo, Y. Chen, J. Kang, J. Wang, W. Huang, and T. Yu, Strain-induced direct-indirect bandgap transition and phonon modulation in monolayer WS₂, Nano Res. **8**, 2562 (2015).

[38] J. Pető, G. Dobrik, G. Kukucska, P. Vancsó, A. A. Koós, J. Koltai, P. Nemes-Incze, C. Hwang, and L. Tapasztó, Moderate strain induced indirect bandgap and conduction electrons in MoS₂ single layers, 2D Mater Appl. **3**, 39 (2019).

[39] C. Ma, J. Yan, Y. Huang, Z. Zheng, and G. Yang, Direct-indirect bandgap transition in monolayer MoS₂ induced by an individual Si nanoparticle, Nanotechnology **31**, 065204 (2019).

[40] C. Robert, D. Lagarde, F. Cadiz, G. Wang, B. Lassagne, T. Amand, A. Balocchi, P. Renucci, S. Tongay, B. Urbaszek, and X. Marie, Exciton radiative lifetime in transition metal dichalcogenide monolayers, Phys. Rev. B **93**, 205423 (2016).

[41] H. Liu, T. Wang, C. Wang, D. Liu, and J. Luo, Exciton radiative recombination dynamics and nonradiative energy transfer in two-dimensional transition-metal dichalcogenides, J. Phys. Chem. C **123**, 10087 (2019).

[42] J. J. Esteve-Paredes, S. Pakdel, and J. J. Palacios, Quenching of Exciton Recombination Unstrained Two-Dimensional Monochalcogenides, Phys. Rev. Lett. **123**, 077402 (2019).

[43] Y. Sun, S. E. Thompson, and T. Nishida, *Strain Effect in Semiconductors: Theory and Device Applications* (Springer, New York, 2010), Chap. 2.

[44] We note that the agreement between the model and the experimental data is less good for the *A* exciton with respect to the *I* exciton. This is caused by the presence of small domes close to the edges of the largest domes (namely, where the *A* exciton

dominates) that adds to the effect of the finite resolution of our optical system and of funneling phenomena.

[45] X. He, H. Li, Z. Zhu, Z. Dai, Y. Yang, P. Yang, Q. Zhang, P. Li, U. Schwingenschlogl, and X. Zhang, Strain engineering in monolayer WS$_2$, MoS$_2$, and the WS$_2$/MoS$_2$ heterostructure, Appl. Phys. Lett. **109**, 173105 (2016).

[46] Z. Jin, X. Li, J. T. Mullen, and K. W. Kim, Intrinsic transport properties of electrons and holes in monolayer transition-metal dichalcogenides, Phys. Rev. B **90**, 045422 (2014).

[47] A. Chernikov, T. C. Berkelbach, H. M. Hill, A. Rigosi, Y. Li, O. B. Aslan, D. R. Reichman, M. S. Hybertsen, and T. F. Heinz, Exciton Binding Energy and Nonhydrogenic Rydberg Series in Monolayer WS$_2$, Phys. Rev. Lett. **113**, 076802 (2014).

[48] The 144-meV difference was evaluated by using $m_K^e = 0.63 m_K^h$ derived from Ref. [26] and considering a binding energy for the *A* exciton equal to 320 meV [47].

[49] H. Yuan, Z. Liu, G. Xu, B. Zhou, S. Wu, D. Dumcenco, K. Yan, Y. Zhang, S.-K. Mo, P. Dudin, V. Kandyba, M. Yablonskikh, A. Barinov, Z. Shen, S. Zhang, Y. Huang, X. Xu, Z. Hussain, H. Y. Hwang, Y. Cui, and Y. Chen, Evolution of the valley position in bulk transition-metal chalcogenides and their monolayer limit, Nano Lett. **16**, 4738 (2016).

Supplemental Material for

Evidence of the direct-to-indirect band gap transition in strained two-dimensional WS₂, MoS₂, and WSe₂

E. Blundo[‡], M. Felici[‡], T. Yildirim[†], G. Pettinari[◊], D. Tedeschi[‡], A. Miriametro[‡], B. Liu[†], W. Ma[†], Y. Lu,[†#], and A. Polimeni[‡,]*

[‡] Dipartimento di Fisica, Sapienza Università di Roma, 00185 Roma, Italy

[†] Research School of Electrical, Energy and Materials Engineering, College of Engineering and Computer Science, The Australian National University, Canberra, ACT 2601, Australia

[◊] Institute for Photonics and Nanotechnologies, National Research Council, 00156 Roma, Italy

[#] ARC Centre of Excellence in Future Low-Energy Electronics Technologies (FLEET) ANU node, Canberra, ACT 2601, Australia

[*] antonio.polimeni@roma1.infn.it

Abstract

In this Supplemental Material we (*i*) show micro-Raman measurements over the dome surface to account for the strain gradient, (*ii*) report the effect of methylpentane capping on the temperature dependence of the dome volume, (*iii*) explain how the funneling effect was taken into account to determine the Γ-K cross-over in the valence band, (*iv*) show results about the direct-to-indirect band gap transition in MoS₂ and WSe₂.

Contents

1. Micro-Raman measurements

The following figure shows a micro-Raman mapping performed along the diameter of the same WS$_2$ dome, whose micro-PL mapping is shown and discussed in Fig. 2 of the main text. Details about micro-Raman measurements are reported in the caption of following Figure S1.
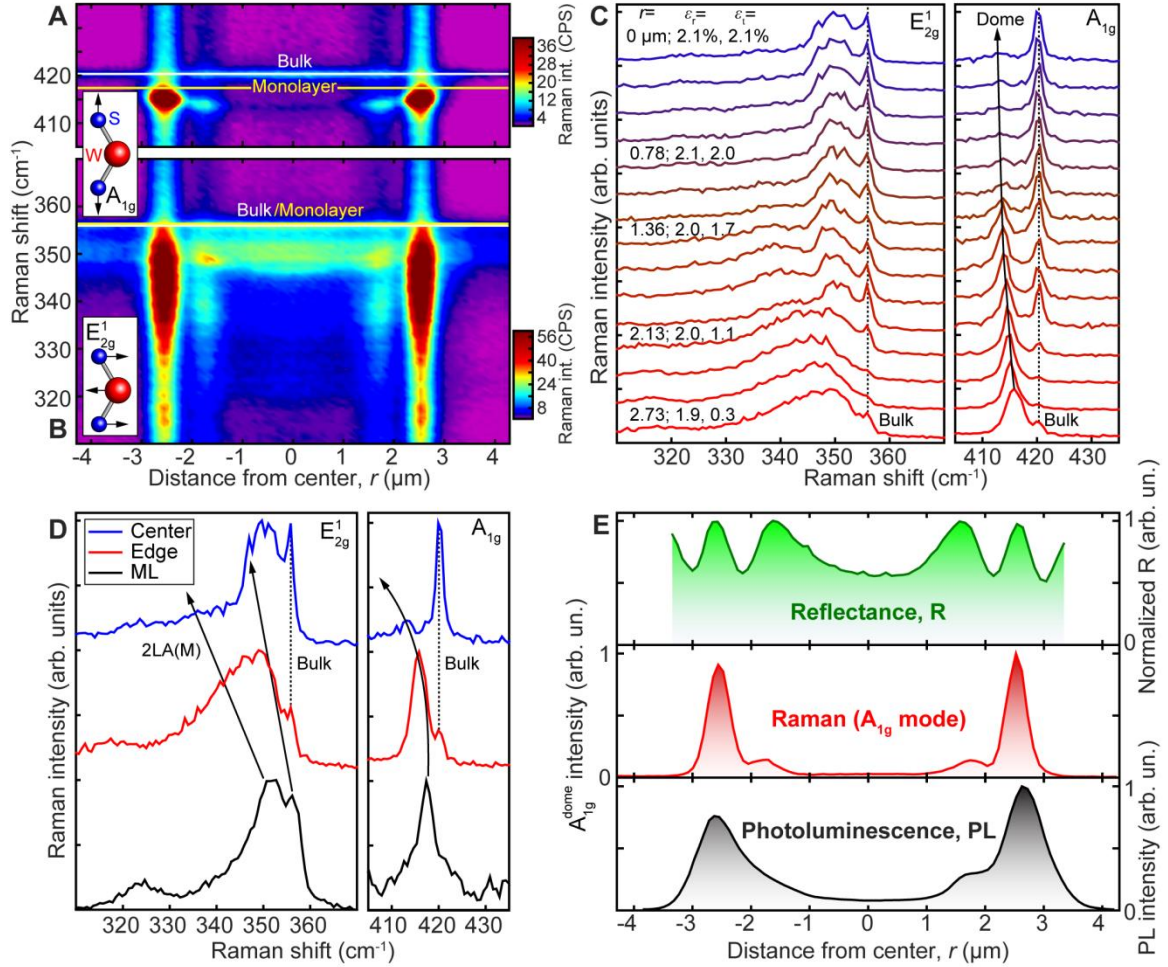

Figure S1. μ-Raman mapping of a WS$_2$ dome

(A) One-dimensional, room-temperature ($T = 297$ K) micro-Raman scan across a WS$_2$ dome, in the spectral region of the A$_{1g}$ phonon mode (the dome is the same one displayed in Fig. 2a of the main text). The horizontal axis indicates the laser spot position with respect to the dome center (r), whereas the vertical axis indicates the Raman shift with respect to the laser line (laser wavelength $\lambda = 532.2$ nm). The micro-Raman intensity is shown in a false color scale (see colorbar). The white (yellow) line marks the position of the A$_{1g}$ mode in bulk (monolayer) WS$_2$[1,2]. **Inset:** Atomic displacements associated with the A$_{1g}$ mode (the vertical axis of the sketch is perpendicular to the monolayer plane). **(B)** Same as Panel A, but for the E$^1_{2g}$ mode. **(C) Left:** Evolution of the normalized micro-Raman spectrum of the dome ($T = 297$ K) in the spectral region of the E$^1_{2g}$ mode, as the laser spot is scanned

1

from the dome's right edge (bottom) to its apex (top). Some selected spectra are labeled with the position of the laser spot and with the values of the radial (ε_r) and circumferential (ε_t) components of the strain tensor (see Fig. 2a of the main text and Supplementary Fig. S1). The dotted line marks the position of the E^1_{2g} mode in bulk WS_2. **Right:** Same as on the left, but for the A_{1g} mode. The black arrow follows the mode shift as the laser is scanned across the dome. **(D)** Right: Comparison between the normalized micro-Raman spectrum ($T = 297$ K) in monolayer WS_2 (bottom) and at the edge (middle) and in the center (top) of the dome, in the spectral region of the E^1_{2g} mode. The dotted line marks the position of the E^1_{2g} mode in bulk WS_2; the arrows follow the Raman shifts of the E^1_{2g} and 2LA(M) modes. The mode at 330 cm^{-1} in the ML spectrum was also observed in Ref. 3. We tentatively ascribe this mode to a LA replica. Right: Same as on the left, but for the A_{1g} mode. **(E)** **Bottom:** Dependence of the integrated micro-PL intensity on the position of the laser spot. In order to obtain the displayed intensity profile, the micro-PL spectra displayed in panels b-c of Fig. 3a in the main text were integrated between 1.7 and 1.95 eV. **Middle:** Evolution of the intensity of the A_{1g} Raman mode as the laser is scanned across the dome. The reported intensity values were obtained by fitting each Raman spectrum (see panel A and the right-hand side of panel C) with the function $I_{tot}=I_{dome}+I_{bulk}+I_{bkg}$. Here, I_{tot} is the total spectrum, whereas I_{bkg} is a flat background. I_{dome} and I_{bulk} are Gaussian functions, respectively taking into account the Raman peaks associated with lattice vibrations in the dome layer and in the underlying bulk WS_2. In the panel we report $I_{dome}+I_{bkg}$, thereby excluding the contribution of bulk WS_2 to the spectrum. **Top:** Normalized reflectance at 532.2 nm as a function of the position of the laser spot. The displayed profile was obtained by collecting the light reflected by the sample as the laser was scanned across the dome, under the same experimental conditions used for micro-Raman and micro-PL measurements (laser wavelength $\lambda = 532.2$ nm, $T = 300$ K, confocal configuration). Note the much different dynamic range spanned by the three intensity profiles with a ratio between the maximal and minimal value equal to 13 and 33 for the micro-PL and micro-Raman profiles, respectively. For micro-PL it is straightforward to ascribe this intensity reduction to the direct-to-indirect band gap transition taking place as one moves from the edge to the center of the dome (see main text, Fig. 2). An analogous behavior to that of the dome discussed in Fig. 2b,c is found also for other WS_2 domes despite of their different dimensions, as also attested by the same ring-like pattern of the laser-excited red luminescence observed for all the domes in Fig. 1c, which suggests a minor role to be played by interference. It seems reasonable to assume a similar origin for the observed reduction of the micro-Raman signal at the dome's center. In this case, some interferential effects can be noticed in between the edge and the center of the dome, where an analogous modulation to that of the reflectance profile can be seen (see, in particular, the minimum for $r \sim \pm 2$ µm). We can therefore conclude that the modulation of the micro-PL and micro-Raman profiles are chiefly due to the strain-induced variations of the electronic properties across the surface of our domes, and interference does not play a primary role.

2. Effects of methylpentane deposition on the *T* dependence of the dome's size

As reported in Ref. 4, the contraction of the H_2 gas trapped inside a dome leads to a progressive reduction of the dome's volume at cryogenic temperatures, which culminates in the dome's disappearance upon reaching the vapor-to-liquid transition temperature at about 32 K. Even though this phenomenon is fully reversible (each dome reappears in its original position when the temperature is increased), the dome's shrinkage at cryogenic temperatures makes it increasingly difficult to spatially resolve the micro-PL signal from different zones of the dome. Also, even if the samples are placed in vacuum in order to achieve low temperatures, this does not lead to a perceptible increase in the volume of the domes. This is due to the fact that the internal pressure for domes with radius $\sim$ 2-3 μm and aspect ratio $h_m/R\sim0.16$ is of about 10 atm[4] or more, at difference with Ref. 5, where domes with $h_m/R\sim0.10$ and internal pressure $\sim$ 1 atm were found to be sensitive to reduction of the external pressure. As noted in the main text, the dome's shrinkage at cryogenic temperatures is potentially highly problematic for time-resolved micro-PL measurements, which must be performed at low temperature to fully appreciate the existing differences in the temporal behavior of the direct and indirect exciton. At room temperature, indeed, non-radiative decay channels dominate the exciton dynamics, as also reported, *e.g.*, in Ref. 6. As illustrated in Fig. S2, however, this issue can be conveniently overcome by covering the sample surface with a thin layer of methylpentane. Indeed, the adhesion of the latter to the dome's walls is enough to nearly stop the dome's contraction with decreasing *T*, without sizably altering the dome's emission properties (see main text).
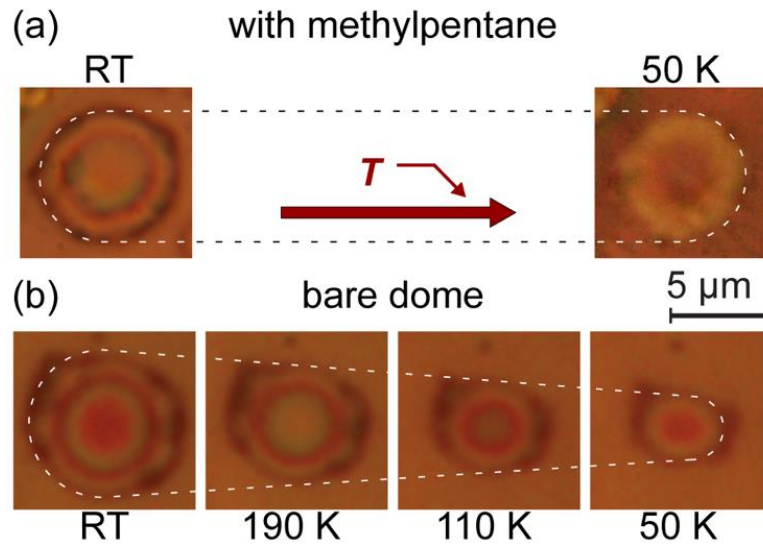
Figure S2. Slowing down the dome's contraction at low *T* by methylpentane deposition

(a) Optical microscope images of the WS_2 dome on which the time-resolved micro-PL measurements discussed in the main text (see Fig. 3) were acquired. The image on the left was acquired at room temperature (*T*~290 K), whereas the image on the right was taken at *T*=50 K (*i.e.,* the temperature at which the time-resolved micro-PL measurements were performed). Even though the same 100× objective (NA=0.75) was used for both images, the quality of the one acquired at *T*=50 K is affected by the aberrations due to the presence of the optical cryostat window in between the objective and the sample. Nevertheless, the effects of methylpentane deposition are clearly visible, *i.e.*, the dome's size becomes nearly insensitive to temperature changes. This is in sharp contrast with the situation depicted in panel (b), which displays the *T* dependence of the dome's size in a "bare" (*i.e.*, not covered with methylpentane) sample. The dome's shrinkage with decreasing *T* is clearly visible in the displayed optical images (acquired with a 50× objective with NA=0.5).

3. Direct-to-indirect band gap transition and funneling effect

First of all, we justify Eq. (1) of the main text, according to which

$$E_{A,I}(\varepsilon_p) = E_{A,I}(0) - \Delta_{A,I} \cdot \varepsilon_p. \tag{S1}$$

In particular, we need to clarify why the energies of the *A* and *I* excitons only depend on the total in-plane strain, $\varepsilon_p = \varepsilon_r + \varepsilon_t$, rather than being an explicit function of the three principal components of the strain tensor, namely

$$E_{A,I}(\varepsilon_r, \varepsilon_t, \varepsilon_z) = E_{A,I}(0) - \left(\Delta^r_{A,I} \cdot \varepsilon_r + \Delta^t_{A,I} \cdot \varepsilon_t + \Delta^z_{A,I} \cdot \varepsilon_z\right) \tag{S2}$$

(it should be noted that the use of the principal components implies that the strain tensor is a diagonal matrix, *i.e.*, there are no shear-strain components to be taken into account). According to Ref. 7, the energy shifts of the first Brillouin-zone critical points of TMD MLs induced by the presence of an in-plane uniaxial tensile strain do not depend heavily on the direction along which the deformation is exerted, so that we can write $\Delta^r_{A,I} \cdot \varepsilon_r + \Delta^t_{A,I} \cdot \varepsilon_t \sim \Delta^p_{A,I} \cdot (\varepsilon_r + \varepsilon_t) = \Delta^p_{A,I} \cdot \varepsilon_p$. Moreover, as we noted in the main text, for biaxially strained TMDs the perpendicular component of the strain tensor can be written as $\varepsilon_z = -\frac{D_{13}}{D_{33}} \varepsilon_p$, where D_{13} and D_{33} are the pertinent components of the elasticity matrix reported in Section 1 of this supplemental Material[8]. As a consequence, Eq. (S2) can be rewritten as

$$E_{A,I}(\varepsilon_p) = E_{A,I}(0) - \left(\Delta^p_{A,I} \cdot \varepsilon_p - \Delta^z_{A,I} \cdot \frac{D_{13}}{D_{33}} \varepsilon_p\right), \tag{S3}$$

which is identical to Eq. (S1) (*i.e.*, to Eq. (1) of the main text), with $\Delta_{A,I} = \Delta^p_{A,I} - \Delta^z_{A,I} \cdot \frac{D_{13}}{D_{33}}$. The validity of Eq. (1) of the main text implies that the analysis of the dependence of $E_{A,I}$ on ε_p can yield important information on the energy bands of WS$_2$—such as the energy of the *I* exciton for zero strain, $E_I(0)$—and on their dependence on strain, quantified through the $\Delta_{A,I}$ energy shift rates. In order to extract this information from the experimental data reported in Fig. 4 of the main text, however, we have to take into account the continuous reduction of the energy gap of the material on going from the edge to the center of the curved dome's surface. As a consequence of this reduction, the photogenerated carriers drift towards the minimum energy available within their diffusion length

5

(funnel effect)[9,10], *i.e.*, towards the dome's center. Combined with the finite exciting/collecting area of the objective, this alters profoundly the correspondence between the coordinate r (and thus ε_p) and the exciton energy resulting from the emission spectra. The curves superimposed on the experimental data in Fig. 4 simulate the local values of the energies of the A and I exciton band gaps. These latter were deduced by a model in which exciton annihilation takes place in the minimum energy available within the objective collection area[10]. For each set of data, the solid line results from a fit performed by fixing the radius of the collection area, R_c, to 2.5σ ($\sigma = 0.23$ µm is the laser spot size; see Ref. 12 in the main text), whereas the shaded areas are delimited by the fitting curves (barely observable) obtained for $R_c = 2\sigma$ and 3σ. This range of R_c—which ultimately sets the uncertainty of our fitting procedure—was chosen to account for the effect of the pinhole used to spatially filter the collected light in our confocal microscope, which was indeed verified to transmit between 95% and 99% of the laser light reflected by the sample. The actual (*i.e.*, free from the funnel effect) strain dependences of the A and I excitons are provided in Fig. 4b by blue and red dashed lines—again computed for $R_c = 2.5\sigma$—and by their corresponding shaded areas, indicating the regions spanned by the theoretical trends in the $2\sigma \leq R_c \leq 3\sigma$ range.

4. Direct-to-indirect band gap transition in MoS2 and WSe2 monolayers

The findings reported for the WS$_2$ dome in the main text are general and were observed in many other WS$_2$ domes and also in other TMD compounds. In the following figure S3, we show the micro-PL spectra recorded in different points of a single MoS$_2$ (left) and WSe$_2$ (right) dome, showing the dramatic changes of the emission spectrum on going from the dome's edge to its center.
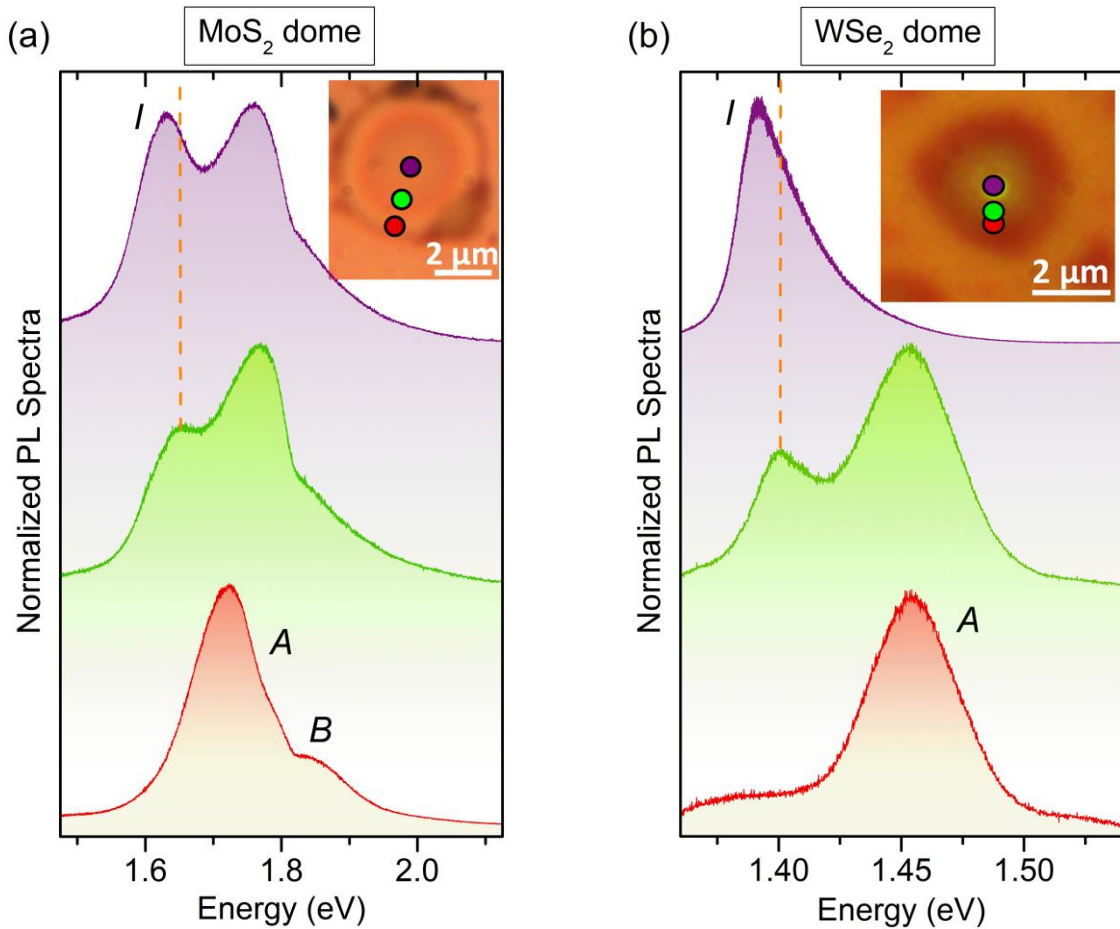

Figure S3. Direct-to-indirect bandgap crossover in MoS2 and WSe2 domes.
(a) Micro-PL spectra acquired in the positions highlighted by the colored dots in the MoS$_2$ dome (with footprint radius R = (2.46±0.06) μm and h_m/R = 0.164) shown as inset. The spectra are peak-normalized for ease of comparison. At the edges of the dome (red dot in the inset and corresponding red spectrum) the main peak is multi-composite and dominated by the direct A exciton (corresponding to the K$_C$-K$_V$ transition). The B exciton involving the conduction band minimum at K$_C$ and the lower split band at K$_V$ in valence band can also be observed. According to our mechanical model, at the edges of MoS$_2$ domes the strain is strongly anisotropic with a radial component equal to ~ 1.5-2 % and an almost null circumferential component (see Ref. 4). For the dome shown here, the radial component at the edges is equal to 1.8 %. The main peak appears to be broad and composite due to:

7

(i) the complex strain distribution coupled to the finite resolution of our optical system (as discussed in the main text) and to funneling phenomena, that broadens the A peak; (ii) contributions from the indirect transition due to the high strains at the edges; (iii) in addition, large domes are often characterized by the presence of small domes at their edges, that may both slightly alter the profile at the edge (and hence the strain distribution) of the larger dome and contribute to the PL emission. These factors are likely responsible for irregular behaviors observed close to the edges of the domes. Notice that deviations from the expected linear behavior towards higher energies were also observed also for uniaxially-strained MoS_2 monolayers in Ref. 11, for strains $\gtrsim$ 1.4 %. In between the edges and the center (see green dot in the inset and corresponding green spectrum) a new band (I) appears, which we attribute to the indirect K_{CB}-Γ_{VB} transition. The A and I bands then redshift while going towards the center, where strain features a more regular biaxial distribution with $\varepsilon_r \approx \varepsilon_t =$ 3.9 %. The I band starts dominating the spectrum at the dome summit (purple dot in the inset and corresponding purple spectrum). Notice that at the center the I and A band are redshifted by about 22 meV and 9 meV, respectively, with respect to the green dot, accordingly to the increase of biaxial strain and the theoretically predicted higher shift rate for the K_{CB}-Γ_{VB} transition with respect to the K_{CB}-K_{VB} transition[7,12,13]. The dashed orange line highlights the redshift of the I exciton. Concomitantly, a reduction in the PL signal is observed, the PL signal at the edge being $\sim$ 10 times more intense than at the center, for the dome shown here. Such an intensity reduction at the center is often even larger, leading to a quenching of the luminescence so that in most of the domes the I band can hardly be observed. The analysis of the shifts of the direct and indirect transitions of single MoS_2 domes is complex due to the irregular behaviors observed at the edges and here discussed. For this reason, a more thorough analysis of the shift of the A and I bands was performed by considering only the spectrum evolution close to the dome summit for the dome shown here and for another dome, featuring an analogous behavior. This analysis was performed similarly to the WS_2 dome presented in the main text (*i.e.*, by fixing $E_A(0)$ to 1.89 eV, the strain-free ML exciton energy[4]) and leads to shift rates equal to 37^{+3}_{-1} and to 91^{+21}_{-13} for the A and I exciton transition, respectively, and to the results summarized in Table I in the main text.

(b) Same as in panel (a) for the WSe_2 dome (with footprint radius $R =$ (1.42±0.06) μm) shown as inset. This dome is among the largest WSe_2 domes we could fabricate. The direct A exciton (corresponding to the K_C-K_V transition) dominates the spectrum at the edges (red dot in the inset and corresponding red spectrum). The indirect I band appears while moving towards the center (green dot and corresponding green spectrum), redshifts while approaching the dome summit (as highlighted by the dashed orange line) and finally dominates the spectrum (purple dot and spectrum). For this compound, no significant quenching of the PL signal is observed for increasing tensile strain, the signal often increasing while going from the edges towards the domes' summit. An increase in the PL emission was also observed in Ref. 14 for WSe_2 monolayer under uniaxial strain. In our domes, however, the signal is observed not to decrease even in presence of the direct-to-indirect bandgap transition (for the dome here shown the signal at the center is found to be almost 10 times higher than at the edges). This enhancement in the PL efficiency is likely aided by funneling effects combined with the small dimensions of the WSe_2 domes we can create: The larger domes have dimensions comparable to that of the excitation laser spot, resulting in funneling of excitons at the dome summit and thus favoring the indirect transition. In addition, interference could play a role in modulating the PL intensity. A thorough analysis was not performed on this compound since it would be

characterized by a too large uncertainty, due to the small dimensions of the dome. In any event, our studies on WSe$_2$ domes suggest that the bandgap crossover occurs for an in-plane strain ~ 2-3 %.

References

1. A. Berkdemir, H. R. Gutiérrez, A. R. Botello-Méndez, N. Perea-López, A. L. Elías, C.-I. Chia, B. Wang, V. H. Crespi, F. López-Urías, J.-C. Charlier, H. Terrones, and M. Terrones, Identification of individual and few layers of WS_2 using Raman Spectroscopy, Sci. Rep. **3**, 1755 (2013).

2. W. Zhao, Z. Ghorannevis, K. K. Amara, J. R. Pang, M. Toh, X. Zhang, C. Kloc, P. H. Tane, and G. Eda, Lattice dynamics in mono- and few-layer sheets of WS_2 and WSe_2, Nanoscale **5**, 9677 (2013).

3. H. Malekpour, and A. Balandin, Raman-based technique for measuring thermal conductivity of graphene and related materials, J. Raman Spectrosc. **49**, 106 (2018).

4. D. Tedeschi, E. Blundo, M. Felici, G. Pettinari, B. Liu, T. Yildrim, E. Petroni, C. Zhang, Y. Zhu, S. Sennato, Y. Lu, and A. Polimeni, Controlled Micro/Nanodome Formation in Proton-Irradiated Bulk Transition-Metal Dichalcogenides, Adv. Mater. **31**, 1903795 (2019).

5. Z. Jia, J. Dong, L. Liu, A. Nie, J. Xiang, B. Wang, F. Wen, C. Mu, Z. Zhao, B. Xu, Y. Gong, Y. Tian, and Z. Liu, Photoluminescence and Raman Spectra oscillations Induced by laser Interference in Annealing-Created Monolayer WS_2 bubbles, Adv. Opt. Mat. **7**, 1801373 (2019).

6. C. Robert, D. Lagarde, F. Cadiz, G. Wang, B. Lassagne, T. Amand, A. Balocchi, P. Renucci, S. Tognay, B. Urbaszek, and X. Marie., Exciton radiative lifetime in transition metal dichalcogenide monolayers, Phys. Rev. B **93**, 205423 (2016).

7. P. Johari and V. B. Shenoy, Tuning the electronic properties of semiconducting transition metal dichalcogenides by applying mechanical strains. ACS Nano **6**, 5449 (2012).

8. Y. Sun, S. E. Thompson, and T. Nishida, Strain Effect in Semiconductors: Theory and Device Applications, Ch. 2 (Springer New York, 2010).

9. J. Feng, X. Qian, and C.-W Huang, Strain-engineered artificial atom as a broad-spectrum solar energy funnel, Nat. Photon. **6**, 865 (2012).

10. A. Castellanos-Gomez, R. Roldán, E. Cappelluti, M. Buscema, F. Guinea, H. S. van der Zant, G. A. Steele, Local Strain Engineering in Atomically Thin MoS_2. Nano Lett. **13**, 5361 (2013).

11. H. J. Conley, B. Wang, J. I. Ziegler, R. F. Haglund Jr., S. T. Pantelides, and K. I. Bolotin, Bandgap engineering of strained monolayer and bilayer MoS_2, Nano Lett. **13**, 3626 (2013).

12 H. Shi, H. Pan, Y.-W. Zhang, and B. I. Yakobson, Quasiparticle band structures and optical properties of strained monolayer MoS_2 and WS_2. Phys. Rev. B **87**, 155304 (2013).

13 C.-H. Chang, X. Fan, S.-H. Lin, and J.-L. Kuo, Orbital analysis of electronic structure and phonon dispersion in MoS_2, $MoSe_2$, WS_2, and WSe_2 monolayers under strain. Phys. Rev. B **88**, 195420 (2013).

14. S. B. Desai, G. Seol, J. S. Kang, H. Fang, C. Battaglia, R. Kapadia, J. W. Ager, J. Guo, and A. Javey, Strain-induced indirect to direct Bandgap transition in multilayer WSe_2, Nano Lett. **14**, 4592 (2014).